The Astrophysical Journal, 867:153 (15pp), 2018 November 10 https://doi.org/10.3847/1538-4357/aae396

No Evidence for Millimeter Continuum Source Overdensities in the Environments of $z \gtrsim 6$ Quasars

Jaclyn B. Champagne[1], Roberto Decarli[2,3], Caitlin M. Casey[1], Bram Venemans[2], Eduardo Bañados[4,12], Fabian Walter[2], Frank Bertoldi[5], Xiaohui Fan[6], Emanuele Paolo Farina[7], Chiara Mazzucchelli[2], Dominik A. Riechers[8], Michael A. Strauss[9], Ran Wang[10], and Yujin Yang[11]
[1] University of Texas at Austin, 2515 Speedway Boulevard, Stop C1400, Austin, TX 78712, USA
[2] Max Planck Institute for Astronomy, Heidelberg, D-69117, Germany
[3] INAF—Osservatorio di Astrofisica e Scienza dello Spazio di Bologna, via Gobetti 93/3, I-40129 Bologna, Italy
[4] The Observatories of the Carnegie Institution for Science, 813 Santa Barbara Street, Pasadena, CA 91101, USA
[5] Argelander Institute for Astronomy, University of Bonn, Auf dem Hügel 71, D-53121 Bonn, Germany
[6] Steward Observatory, University of Arizona, Tuscon AZ, 85721, USA
[7] Department of Physics, University of California, Santa Barbara, CA 93106, USA
[8] Cornell University, 220 Space Sciences Building, Ithaca, NY 14853, USA
[9] Department of Astrophysical Sciences, Princeton University, Princeton, NJ 08544 USA
[10] Kavli Institute of Astronomy and Astrophysics at Peking University, No. 5 Yiheyuan Road, Haidian District, Beijing 100871, People's Republic of China
[11] Korea Astronomy and Space Science Institute, 776 Daedeokdae-ro, Yuseong-gu, Daejeon 34055, Republic of Korea
Received 2018 June 29; revised 2018 September 5; accepted 2018 September 20; published 2018 November 12

Abstract

Bright high-redshift quasars ($z > 6$) hosting supermassive black holes ($M_{\rm BH} > 10^8\,M_\odot$) are expected to reside in massive host galaxies embedded within some of the earliest and most massive galaxy overdensities. We analyze 1.2 mm ALMA dust continuum maps of 35 bright quasars at $6 < z < 7$ and search the primary beam for excess dust continuum emission from sources with $L_{\rm IR} \gtrsim 10^{12}\,L_\odot$ as evidence for early protoclusters. We compare the detection rates of continuum sources at $\geqslant 5\sigma$ significance in the fields surrounding the quasars ($A_{\rm eff} = 4.3$ arcmin^2) with millimeter number counts in blank field surveys. We discover 15 mm sources in the fields excluding the quasars themselves, corresponding to an overdensity of $\delta_{\rm gal} \equiv (N_{\rm gal} - N_{\rm exp})/N_{\rm exp} = -0.07 \pm 0.56$, consistent with no detected overdensity of dusty galaxies within 140 physical kpc of the quasars. However, the apparent lack of continuum overdensity does not negate the hypothesis that quasars live in overdense environments, as evidenced by strong [C II] overdensities found on the same scales as similarly selected quasars. The small field of view of ALMA could miss a true overdensity if it exists on scales larger than 1 cMpc, if the quasar is not centered in the overdensity, or if quasar feedback plays a role close to the quasar, but it is most likely that the large line-of-sight volume probed by a continuum survey will wash out a true overdensity signal. We discuss the necessary factors in determining the bias with which dusty star-forming galaxies trace true dark matter overdensities in order to improve upon overdensity searches in the dust continuum.

Key words: galaxies: high-redshift – large-scale structure of universe – quasars: general

1. Introduction

The processes by which dusty star-forming galaxies within large-scale structure collapse and evolve over time are unconstrained both in theory (Narayanan et al. 2015; Chiang et al. 2017) and in observations (Chapman et al. 2009; Casey 2016). Cosmological simulations in a cold dark matter universe show that structures form hierarchically, i.e., that the earliest structures should be less massive than the galaxy clusters and superclusters we see today (Springel et al. 2005). However, cosmic downsizing (Cowie & Hu 1986) suggests that the most massive structures in overdense environments assembled their mass earlier than galaxies in the surrounding field, thus making high-redshift observations critical for studying the progenitors of galaxy clusters seen in the present universe. It remains observationally unclear when in cosmic history the seeds of these clusters took root and what the evolutionary processes were therein.

The highest-redshift quasars ($z > 6$) host supermassive black holes, where $M_{\rm BH} \gtrsim 10^8\,M_\odot$ (e.g., De Rosa et al. 2011; Mazzucchelli et al. 2017b). Theoretical models suggest that they reside in massive host galaxies that are located in some of the highest overdensities at these early cosmic epochs (Overzier et al. 2009; Costa et al. 2014; Sijacki et al. 2015) and grow rapidly at these times through super-Eddington accretion (Madau et al. 2014; Pezzulli et al. 2017). Galaxy clusters seen at present times are dominated by massive, old elliptical galaxies (Lewis et al. 2002; Skibba et al. 2009), which must have assembled much faster than those in the field. If indeed these massive galaxies coalesced more quickly, we would expect to detect their high-redshift progenitors as highly dust-obscured sources in regions of massive overdensities.

Thousands of quasi-virialized[13] galaxy clusters, marked by spatially extended X-ray bremsstrahlung and millimeter Sunyaev–Zel'dovich signatures of a hot intracluster medium (ICM), have been confirmed in the $z < 1.5$ universe (Allen et al. 2011; Kravtsov & Borgani 2012). But protoclusters that have not yet collapsed do not exhibit strong ICM emission or absorption, and have typically been identified via overdensities of star-forming galaxies. For instance, evidence for massive overdensities and protoclusters at $z > 2$ has been found through Lyman-break galaxies (LBGs; Steidel et al. 1998, 2005;

---

[12] Carnegie-Princeton Fellow.

[13] The most massive galaxy clusters are closest to virialization, but generally $z = 0$ clusters are still not fully virialized beyond the core; see Xu et al. (2000).

Capak et al. 2011; Riechers et al. 2014), Lyα emitters (LAEs) via narrowband imaging (Venemans et al. 2002, 2005b; Bădescu et al. 2017; Toshikawa et al. 2018), and dusty star-forming galaxies via cold dust emission (Chapman et al. 2009; Chiang et al. 2013; Casey et al. 2015; Casey 2016; Hung et al. 2016). The FORS2 instrument on the Very Large Telescope (VLT; Appenzeller et al. 1998) as well as Suprime-Cam on the Subaru telescope (Miyazaki et al. 2002) have been instrumental in the detection and imaging of LAE overdensities at $z > 4$ (e.g., Shimasaku et al. 2003; Venemans et al. 2005b; Kuiper et al. 2011).

Similar searches have been performed looking for UV-selected galaxies at higher redshifts, specifically around $z \geqslant 5$ quasars, using both narrowband imaging (e.g., Bañados et al. 2013; Goto et al. 2017; Mazzucchelli et al. 2017a; Ota et al. 2018) and spectroscopy (e.g., Farina et al. 2017). Yet many of them have yielded inconclusive results about the true nature of quasar environments; some searches for LAEs as proof of clustering around quasars have revealed a puzzling lack of overdensities. This has opened questions about the field of view and depth necessary to probe real overdensities (see also Stiavelli et al. 2005), but one should note that narrowband searches can be particularly hampered by low sensitivity as well as the uncertainty in the redshift of the quasar, which could lead to companions falling out of the narrowband entirely. Farina et al. (2017) finds an LAE at very close proximity to quasar J0305–3150 using the multi-unit spectroscopic explorer on the VLT, which would have been missed by narrow-band searches due to sensitivity constraints.

The advantages of Lyα in particular are that it is selected in a narrow redshift range in narrowband imaging, and it can presently be detected out to $z \sim 7$, so it can be used as a reliable redshift measure in the earliest massive overdensities (e.g., Djorgovski et al. 1985; Palunas et al. 2004). At the highest redshifts ($z > 7$), single detections of LAEs with large equivalent widths may be indications of ionizing regions around protoclusters (Larson et al. 2018). However, individual Lyα studies are observationally expensive, as optical observations of LAEs in dense environments becomes challenging due to increasing absorption of Lyα by the neutral intergalactic medium (IGM) at the highest redshifts (Treu et al. 2013). Fortunately, studies in longer wavelength emission are not so severely impacted by the neutral IGM.

Infrared (IR) emission lines like [C II] (158 μm) serve as a robust redshift tracer of the interstellar medium. Recent studies of atomic gas in the vicinity of high-redshift quasars include Decarli et al. (2017), which discovered an overdensity of galaxies in [C II] around quasars in a sample that overlaps with that presented here. From this sample, Decarli et al. present bright, gas-rich, star-forming galaxies at the same redshift as the quasars in four fields (two of which also have strong continuum emission) concluding that this is consistent with a local peak in the overall galaxy number counts in [C II]. ALMA observations have revealed a number of millimeter continuum and [C II] companions near $z \sim 5$ (Trakhtenbrot et al. 2018) and $z \sim 6$ quasars (Willott et al. 2017). Here, we focus on the number counts of dust continuum sources surrounding the quasar environment, which provide a direct measure of star formation activity in galaxies at $z \sim 6$. Millimeter continuum allows us to probe a larger redshift range than in [C II], which can additionally be very faint compared to the far-IR luminosity. Searching specifically for dust continuum sources should provide a complementary data set to [C II] studies that could trace these detected overdensities, as it is likely that galaxies with strong [C II] signatures indicative of star formation would contain a significant amount of dust.

While [C II] provides precise redshift information, dust statistics probe a much larger line-of-sight volume, allowing for considerable foreground projection. However, the number counts for 1.1 and 1.2 mm sources are more certain than high-redshift UV, IR, and [C II] luminosity functions (e.g., Finkelstein et al. 2015; Aravena et al. 2016b), so we would not need to detect an extreme (i.e., orders of magnitude) excess of galaxies in order to find robust evidence for protoclusters. Without spectroscopic redshifts, the hypothesis of this study is that a high number of millimeter dust emitters found in close angular proximity to the high-redshift quasars, as compared with randomly chosen blank fields, could provide statistical evidence for clustering at early times. Other studies lacking redshifts, including radio continuum (e.g., Carilli et al. 2004) and using the Lyman-break technique (e.g., Kim et al. 2009), have been unable to confirm physical association with the quasar, but an overdensity of sources beyond small number statistics would be evidence for early protoclusters, similar to the LBG overdensity detected in the protocluster TN J1338 (Miley et al. 2004) as well as the submillimeter mapping of radio galaxies and their companions (Stevens et al. 2003).

The increasing sample size of high-redshift quasars opens a particularly interesting avenue for protocluster detections at longer wavelengths, in complement to the LAE searches. The number of confirmed bright $z > 6$ quasars has significantly increased recently through large-area sky surveys (e.g., Bañados et al. 2014, 2016; Jiang et al. 2016; Matsuoka et al. 2016; Mazzucchelli et al. 2017b; Reed et al. 2017), and many of these have been observed in millimeter wavelengths (e.g., Decarli et al. 2018). Thus, for the first time we have a sufficiently large statistical basis for a search for possible overdensities of dusty, gas-rich galaxies in their surrounding environment at very high redshifts. Additionally, the ALMA era has made it possible to find faint sources in continuum at very high redshift ($z > 5$–6).

In this study we examine the primary beams of high-redshift quasar pointings from ALMA Cycles 0–4 and compare them with the number counts of sources in blind surveys, providing a unique constraint on whether dust continuum traces the overdensities already known to be present in [C II]. In Section 2 we describe the observations and data reduction, in Section 3 we give details on the analysis of the images and calculation of the number counts, and in Sections 4 and 5 we give a discussion and concluding remarks. We assume the *Planck* cosmology with a flat universe, with $H_0 = 67.77$ km s^{-1} Mpc^{-1} and $\Omega_m = 0.308$ (Planck Collaboration et al. 2016).

2. Observations and Data Reduction

We examine 35 quasars spanning $5.95 < z < 6.90$ with ALMA observations in Band 6 (211–275 GHz, corresponding to rest-frame FIR ~150–200 μm). Eight of the quasars are archival observations from Cycles 0 and 1. The remaining 27 objects constitute the sample used in the [C II] search by Decarli et al. (2017, 2018). Thus, these observations have spectral windows encompassing the expected observed frequency of [C II]. They were carried out between 2016 January and July, with a compact configuration using 38–49 12 m antennas. The primary beam of ALMA in Band 6 is about 25″

Table 1

List of Properties for the Quasar Targets

Target Name (1)	Short Name (2)	R.A. (J2000) (3)	Decl. (J2000) (4)	$\sigma_{\rm cont}$ (μJy) (5)	z (6)	Redshift Method (7)	References (8)
PSO J007.0273+04.9571	PJ007+04	00:28:06.56	+04:57:25.68	87.4	6.00 ± 0.05	[C II]	1
PSO J009.7355–10.4316	PJ009–10	00:38:56.522	−10:25:53.90	84.9	5.95 ± 0.05	[C II]	1
VIK J0046–2837	J0046–2837	00:46:23.65	−28:37:47.34	70.8	5.9900 ± 0.05	[C II]	2
VIK J0109–3047	J0109–3047	01:09:53.13	−30:47:26.3	44.2	6.7909 ± 0.0004	[C II]	15
ATLAS J025.6821–33.4627	J0142–3327	+01:42:43.73	−33:27:45.47	61.2	6.31 ± 0.03	Lyα	3
CFHQS J0210–0456	J0210–0456	02:10:13.19	−04:56:20.9	28.3	6.4323 ± 0.0005	[C II]	14
VIK J0305–3150	J0305–3150	03:05:16.92	−31:50:56.0	44.0	6.6145 ± 0.0001	[C II]	15
PSO J065.4085–26.9543	PJ065–26	04:21:38.052	−26:57:15.60	60.9	6.14 ± 0.05	[C II]	1
PSO J065.5041–19.4579	PJ065–19	04:22:00.994	−19:27:28.68	46.6	6.12 ± 0.05	[C II]	1
VDES J0454–4448	J0454–4448	04:54:01.79	−44:48:31.1	46.1	6.10 ± 0.01	[C II]	4
SDSS J0842+1218	J0842+1218	08:42:29.429	+12:18:50.50	43.0	6.069 ± 0.002	MgII	5
SDSS J1030+0524	J1030+0524	10:30:27.098	+05:24:55.00	53.4	6.308 ± 0.001	MgII	6
PSO J159.2257–02.5438	PJ159–02	10:36:54.191	−02:32:37.94	60.7	6.38 ± 0.05	[C II]	1
VIK J1048–0109	J1048–0109	10:48:19.086	−01:09:40.29	60.0	6.6610 ± 0.005	MgII	2
PSO J167.6415–13.4960	PJ167–13	11:10:33.976	−13:29:45.60	43.7	6.508 ± 0.001	MgII	7
ULAS J1148+0702	J1148+0702	11:48:03.286	+07:02:08.3	55.4	6.339 ± 0.001	MgII	8
VIK J1152+0055	J1152+0055	11:52:21.269	+00:55:36.69	54.5	6.3700 ± 0.01	Lyα	9
ULAS J1207+0630	J1207+0630	12:07:37.440	+06:30:10.37	53.1	6.040 ± 0.003	Lyα	8
PSO J183.1124+05.0926	PJ183+05	12:12:26.981	+05:05:33.49	62.3	6.4386 ± 0.0004	[C II]	1
SDSS J1306+0356	J1306+0356	13:06:08.258	+03:56:26.30	57.5	6.016 ± 0.002	MgII	6
ULAS J1319+0950	J1319+0950	13:19:11.29	+09:50:51.4	60.7	6.133 ± 0.0012	CO	13
PSO J217.0891–16.0453	PJ217–16	14:28:21.394	−16:02:43.29	68.9	6.11 ± 0.05	[C II]	1
CFHQS J1509–1749	J1509–1749	15:09:41.778	−17:49.26.80	57.9	6.121 ± 0.002	MgII	10
PSO J231.6576–20.8335	PJ231–20	15:26:37.841	−20:50:00.66	98.4	6.5950 ± 0.015	[C II]	11
PSO J308.0416–21.2339	PJ308–21	20:32:09.996	−21:14:02.31	27.7	6.24 ± 0.05	[C II]	1
SDSS J2054–0005	J2054–0005	20:54:06.49	−00:05:14.8	30.7	6.0391 ± 0.0022	CO	13
CFHQS J2100–1715	J2100–1715	21:00:54.616	−17:15:22.50	49.0	6.087 ± 0.005	MgII	10
VIK J2211–3206	J2211–3206	22:11:12.391	−32:06:12.94	48.3	6.3360 ± 0.005	MgII	2
PSO J340.2041–18.6621	PJ340–18	22:40:48.997	−18:39:43.81	61.1	6.01 ± 0.05	[C II]	1
SDSS J2310+1855	J2310+1855	23:10:38.88	+18:55:19.7	51.7	6.0031 ± 0.0007	CO	13
VIK J2318–3029	J2318–3029	23:18:33.100	−30:29:33.37	94.4	6.1200 ± 0.05	[C II]	2
VIK J2318–3113	J2318–3113	23:18:18.351	−31:13:46.35	86.7	6.4440 ± 0.005	MgII	2
CFHQS J2329–0301	J2329–0301	23:29:08.28	−03:01:58.8	21.0	6.417 ± 0.002	MgII	14
VIK J2348–3054	J2348–3054	23:48:33.34	−30:54:01.0	51.9	6.9018 ± 0.0007	[C II]	15
PSO J359.1352–06.3831	PJ359–06	23:56:32.455	−06:22:59.26	94.1	6.15 ± 0.05	[C II]	1

Note. (1) Original target name; (2) short name used throughout this paper; (3)–(4): R.A. and decl. (J2000); (5) continuum rms before primary beam correction (μJy); (6) redshift; (7) method for redshift determination; (8) redshift references.

References. (1) Bañados et al. (2016), (2) B. P. Venemans et al. (2018, in preparation), (3) Carnall et al. (2015), (4) Reed et al. (2017), (5) De Rosa et al. (2011), (6) Kurk et al. (2007), (7) Venemans (2015), (8) Jiang et al. (2016), (9) Matsuoka et al. (2016), (10) Willott et al. (2010), (11) Mazzucchelli et al. (2017a), (12) Kurk et al. (2009), Willott et al. (2009), (13) Wang et al. (2013), (14) Willott et al. (2013), (15) Venemans et al. (2013).

at FWHM, corresponding to an angular diameter distance of $\sim$140 physical kpc, or $\sim$1.0 comoving Mpc, at $z \sim 6.5$, a representative redshift for the sample.

The quasars in our sample were originally identified in multiple optical and near-IR surveys including the Sloan Digital Sky Survey (SDSS; Jiang et al. 2016), Pan-STARRS1 (Bañados et al. 2016), VIKING (Venemans et al. 2013), ATLAS (Carnall et al. 2015), CFHQS (Willott et al. 2007), UKIDSS (Mortlock et al. 2009), and VDES (Reed et al. 2017). The sample includes the 27 ALMA observations from Decarli et al. (2017) as well as 8 quasars with archived observations from Cycles 0–1. This study includes every $z \sim 6$ quasar with available Band 6 observations, but is not formally complete in any physical quantity. These quasars were selected via detection in rest-frame UV at 1450 Å (absolute magnitudes <-25 mag), and many of them have had extensive sub/millimeter follow-up and most are hallmarked by strong [C II] detections and very bright ($>$1 mJy) continuum emission in follow-up observations. Table 1 lists the information on the quasars and the details on the ALMA observations used here.

The data have been reduced using the pipeline developed for the Common Astronomy Software Applications (CASA; McMullin et al. 2007) and deconvolved using the CLEAN task. Each data set is imaged using natural weighting and is cleaned down to the 3σ noise level. The pixel size is $0\farcs1 \times 0\farcs1$ for the Cycle 4 data and $0\farcs15 \times 0\farcs15$ for the earlier cycles. The average rms noise in the images is $58.6 \pm 19.0\,\mu$Jy beam^{-1}, spanning a range of 21.0–98.4 μJy beam^{-1}. This is the uncorrected rms calculated from the image after the quasar has been masked out, but before we make the primary beam correction. The typical FWHM of the synthesized beam at these frequencies ranges from $0\farcs5$ to $1\farcs0$. We utilize the original resolution of each map, since homogenizing the resolution across the maps would cause an overall loss of depth. Moreover, the sizes of submillimeter galaxies are

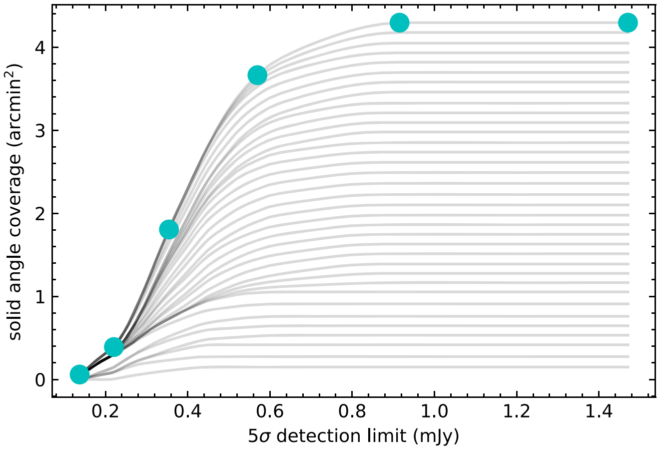

Figure 1. Area covered by this survey as a function of the flux to which it is sensitive at 5σ. Each gray line represents the cumulative solid angle covered by each additional quasar, up to the full sample of 35. The points are binned according to the areas used in calculating the number counts.

expected to be $<0\farcs5$ at $z\sim2.5$ (Hodge et al. 2016), therefore we expect all sources to be unresolved given these beam sizes.

We search for sources only where the primary beam response is greater than 50%, so the final images have been trimmed to this area (approximately $12''$ in radius). Figure 1 shows the total solid angle coverage of our search as a function of the 5σ detection threshold, accounting for the primary beam and that each observation has a different depth. We discuss in Section 3 the choice of the 5σ detection threshold. The deepest data have a flux limit of 0.15 mJy beam^{-1} and the maximum effective area is 4.3 arcmin^2.

3. Data Analysis

We first search for a statistical excess of flux in each quasar field. We exclude the region of the field containing most of the quasar's flux by applying a conservative $4''\times4''$ mask centered on the known quasar coordinates. In the case of J1152+0055, we increased the mask to a radius of $3''$ to exclude extended emission from the quasar host galaxy, as our source-finding algorithm detected significant flux on the border of this mask. In the case of PJ231–20, there was a bright [C II] detection in Decarli et al. (2017) within $2''$ of the quasar so we decreased the mask to a radius of $1\farcs5$. Besides PJ231–20, we consider separate sources only as detections at an angular distance $>2''$ ($\approx$14 pkpc) from the published position of the quasar. We perform this analysis on maps that have not been corrected for the primary beam, so that our source-finding algorithm does not interpret outer-edge pixels with higher noise to be true sources. This cut, in combination with a high signal-to-noise (S/N) threshold, should prevent spurious noise detections. In addition, we address completeness and contamination via mock observations.

If there are zero sources in addition to the quasar in a cleaned primary beam, one would expect a Gaussian distribution of pure noise reflective of the rms of the observations. To make a statistical statement about the excess flux in these fields, we construct a composite histogram of the total flux in the unmasked pixels in each of the maps. We convert the unmasked pixel fluxes to S/N to account for both the primary beam and the different depths of each observation. In Figure 2 we show the distribution of the flux in these masked maps. Since negative flux is guaranteed to be noise, we invert this distribution to show what a pure noise distribution would look like, as compared with the clear statistical positive excess of millimeter flux in all of the fields, with the tail extending fairly bright (S/N > 5). We then search for discrete sources, since interferometic observations filter out diffuse emission through the synthesized beam. Figure 2 also shows the distribution of the flux with both the quasar and the formally detected 5σ sources masked out (this threshold is explained below). This distribution is consistent with a slight positive tail indicating a few sources below the 5σ detection threshold, but we do not include them in our measurements due to our estimation of the contamination. The distribution in Figure 2 suggests that our argument for searching for formally detected discrete sources rather than statistical flux excess is sound.

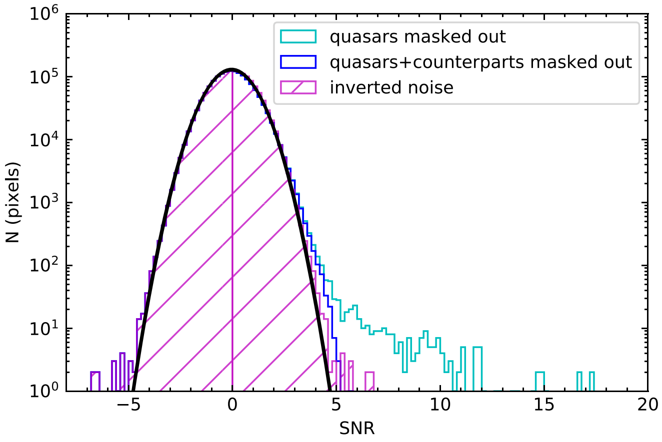

Figure 2. Distribution of the flux in the 35 fields after the target quasars have been masked out. The cyan histogram shows the total remaining flux in all of the quasar-masked maps. The blue histogram shows the remaining flux in the maps with both the quasar and the formally detected sources masked out (see Section 3). The hatched magenta histogram shows the negative flux inverted on the positive side to emphasize the positive excess in the total masked area. The black curve is a Gaussian fit to the noise with the expected $\mu=0$ and $\sigma=1$.

We create S/N maps to identify potential candidates in the field by dividing by the continuum rms (not corrected for the primary beam). In order to find an optimal S/N threshold, we generate 1000 simulated maps with area equivalent to the 35 primary beams in this study. These maps are created with a Gaussian noise distribution, with σ allowed to vary within the range of the rms values in our data. They are convolved with a model ALMA beam of $0\farcs8\times0\farcs5$—for simplicity, we use a single beam-shape typical of these data rather than the full range, since recovering point sources was not sensitive to the beam size we chose. The maps are injected randomly with sources according to a Schechter (1976) function distribution representative of blank field number counts (it is not necessary to account for confusion since the rms in the maps is well above the ALMA confusion limit). We assume the injected sources are unresolved and unclustered. The Schechter model we choose is based on the most recent blank field 1.2 mm number counts compilation of Fujimoto et al. (2016) valid for flux densities of 0.1–1.5 mJy:

$$\frac{dN}{d\log S}=\ln(10)\,\phi_*\left(\frac{S}{S_*}\right)^{\alpha+1}\exp\left(-\frac{S}{S_*}\right), \qquad (1)$$

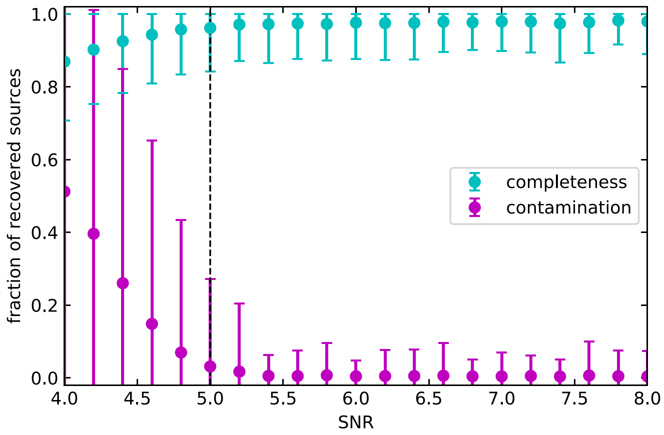

Figure 3. Results from 1000 simulated ALMA maps with sources injected according to blank field estimates. The magenta points show the contamination, i.e., the false detection rate. The cyan points indicate the ratio of recovered legitimate sources to the number of injected sources. The error bars are the 1σ standard deviation in the 1000 maps. We choose an S/N threshold of 5σ based on these results.

where $\phi_* = 1.54^{+0.29}_{-0.26} \times 10^3\ \mathrm{deg}^{-2}\ \mathrm{mJy}^{-1}$, $\alpha = -2.12^{+0.07}_{-0.06}$, and $S_* = 2.35^{+0.16}_{-0.16}$ mJy. Figure 3 shows the completeness (fraction of recovered sources that match the injected sources) and the contamination (fraction of extracted sources that are false) after searching the simulated noise maps for the injected sources using a region-growing algorithm. We convert each simulation from flux density to S/N by dividing by the rms noise in each iteration, which is allowed to vary within 1σ from the average rms in our real maps. The error bars reflect the 1σ standard deviation of the completeness or contamination in all 1000 maps. Figure 3 indicates that we reach a satisfactory completeness of 91.6% and contamination of 4.3% at a 5σ detection threshold. After choosing this S/N threshold, we feed the real S/N maps to the same region-growing algorithm that identifies neighboring pixels in the map above the given threshold. A grouping is declared a source if there are two or more adjacent pixels above the S/N threshold.

4. Results

The results from the source-finding algorithm reveal a total of 15 candidate detections in the 35 fields, none of which are resolved. Contour plots showing the source detections in the quasar-masked fields are displayed in Figure 4, while three [C II] sources found in Decarli et al. (2017) and Willott et al. (2017) are not found in continuum here are shown in Figure 5. The remaining maps that have no additional sources are displayed in Figure 8 in the Appendix. In Table 2 we list the coordinates and primary beam-corrected fluxes of each source. Since these are continuum flux densities, we lack redshifts for these sources so we do not make a statement about the total IR luminosity or the star formation activity in these sources.

For comparison with what is observed in blank fields, we construct the number counts as in previous ALMA surveys (e.g., Fujimoto et al. 2016). The contribution of an identified source of flux density S to the total number counts, ξ, is

$$\xi(S) = \frac{1 - f(S)}{C(S)A_{\mathrm{eff}}(S)}, \tag{2}$$

where $f(S)$ is the contamination factor at 5σ from Figure 3, $C(S)$ is the level of completeness (Figure 3), and A_{eff} is the effective area of our search at flux density S, from Figure 1.

The sum of the contributions in each bin of flux width $\Delta \log S$ is thus

$$n(S) = \frac{\Sigma\xi(S)}{\Delta \log S}. \tag{3}$$

The number counts are thus constructed in six log bins of $\Delta \log S_\nu = 0.25$, divided by the area sensitive to that flux level and corrected for both completeness and contamination. Table 3 lists the values used for the number counts in this work. The uncertainty is calculated based on Poisson statistics propagated with the 1σ uncertainty in the completeness and contamination as from our simulations. We compare the distribution of our sources in Figure 6 with several blank field number counts at 1.1 and 1.2 mm, with fits from Scott et al. (2010) and Fujimoto et al. (2016). The Fujimoto et al. (2016) curve is given along with 16th and 84th percentile values calculated from a Monte Carlo simulation, and the results from our simulations are plotted with the same limits. We calculate an overdensity factor defining $\delta_{\mathrm{gal}} = (N_{\mathrm{gal}} - N_{\mathrm{exp}})/N_{\mathrm{exp}}$. According to the Fujimoto et al. (2016) model, we would expect $N_{\mathrm{exp}} = 16.1^{+3.3}_{-6.8}$ sources between 0.1–10 mJy in these fields without an overdensity, based on the effective area in each bin. Correcting for fidelity and completeness, our measured number of sources, N_{gal}, is 15.1 ± 5.7. Therefore, this implies a value of $\delta_{\mathrm{gal}} = -0.07 \pm 0.56$, consistent with the expected number of sources in the field. Thus, we find that 15 sources in a total area of 4.3 arcmin^2 do not point to an overdensity of 1.2 mm sources with respect to the foreground.

Figure 7 shows the observed and expected number of sources as a function of radial distance from the quasar in a given field. N_{gal} has been recalculated with each field cut to some radius r from the quasar (and the area corrected for sensitivity as before). The sources are consistent with a uniform distribution at 50% of the primary beam, and this remains true at any area cut. The observed number of sources is consistent with the scatter of the expected number of observed sources regardless of area cut, thus showing that our choice of area has not influenced the calculation of the overdensity, and that our measurements are not the result of a poor cleaning procedure.

5. Discussion

Since the number is nearly indistinguishable from the expectations from blank fields, $N_{\mathrm{exp}} = 16.1^{+3.3}_{-6.8}$, there is no statistical overdensity of dust continuum emitters around these quasars. However, we argue that this is not firm evidence for a lack of clustering or large-scale structure around these sources, nor evidence that dust emitters do not exist in protoclusters at these redshifts. The significant result published by Decarli et al. (2017) shows that [C II] overdensities exist extremely close to the quasar, but this need not be evident in all tracers. There are a number of reasons for a lack of close-by continuum detections:

ALMA field of view versus the size of protoclusters. At $z \approx 6$, the ALMA Band 6 primary beam (25″) corresponds only to ~1 comoving Mpc (cMpc) scales, whereas protoclusters are expected to span ~20 cMpc along a side, or 2–3 cMpc in their cores (Overzier et al. 2009; Chiang et al. 2017), since they have not yet virialized in a compact form. Thus, the small field of view of ALMA may miss the presence of a true overdensity, as dust emitters could sit within a large-scale

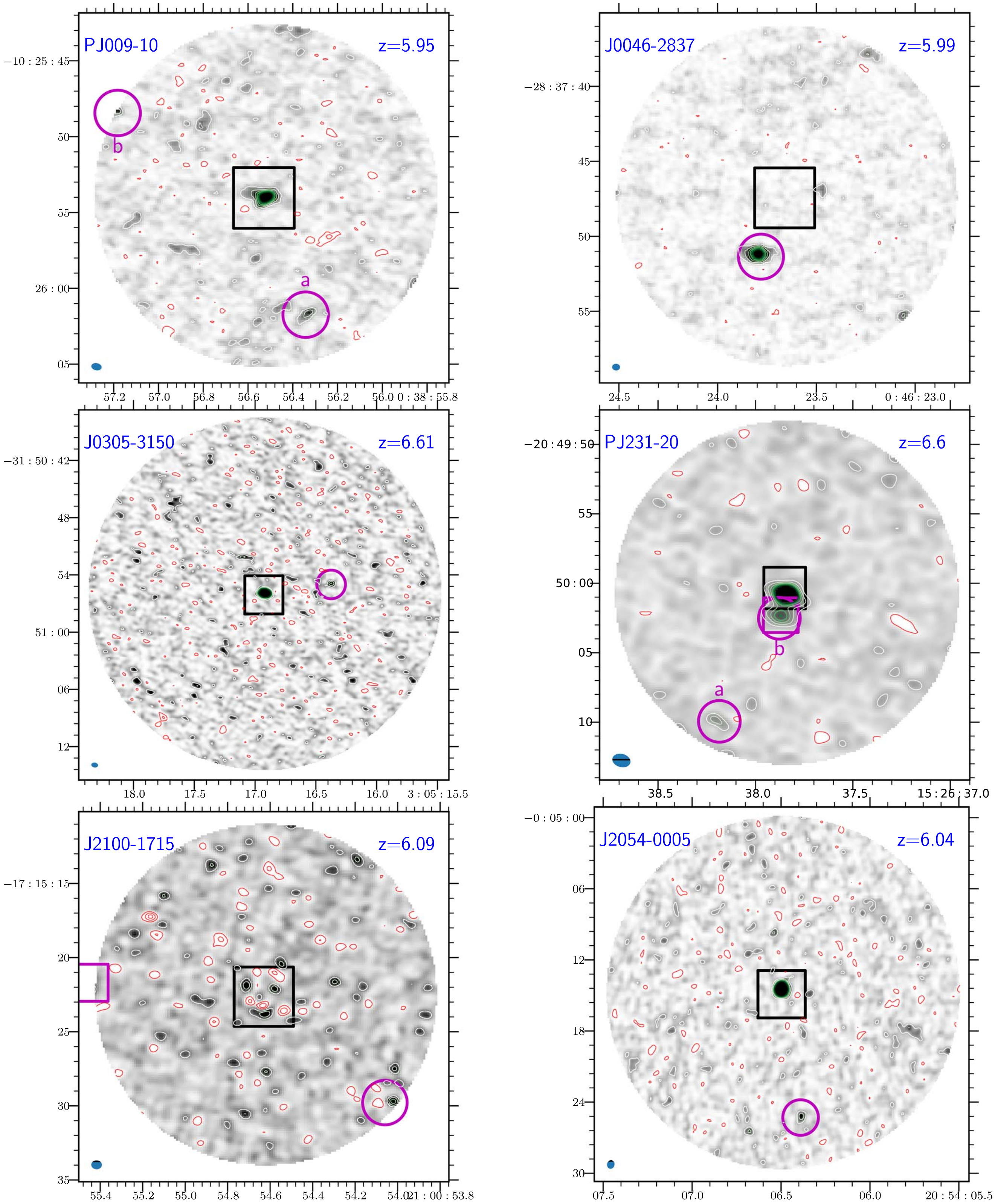

Figure 4. Each map is the cleaned ALMA continuum image within the area of 50% of the primary beam response, with a 16 arcsec^2 mask centered on the quasar. The synthesized beam is displayed in the lower left corner. The red (negative) and green (positive) contours begin at $S/N = |2|$ and step in increments of ± 2. The magenta circles indicate 5σ continuum detections as listed in Table 2 and the squares show where Decarli et al. (2017) found [C II] detections in the same fields. Note that the [C II] detection in the field of J2100–1715 corresponds to a continuum detection in our study but sits outside the 50% primary beam cut, so is not included as a detection in Table 2.

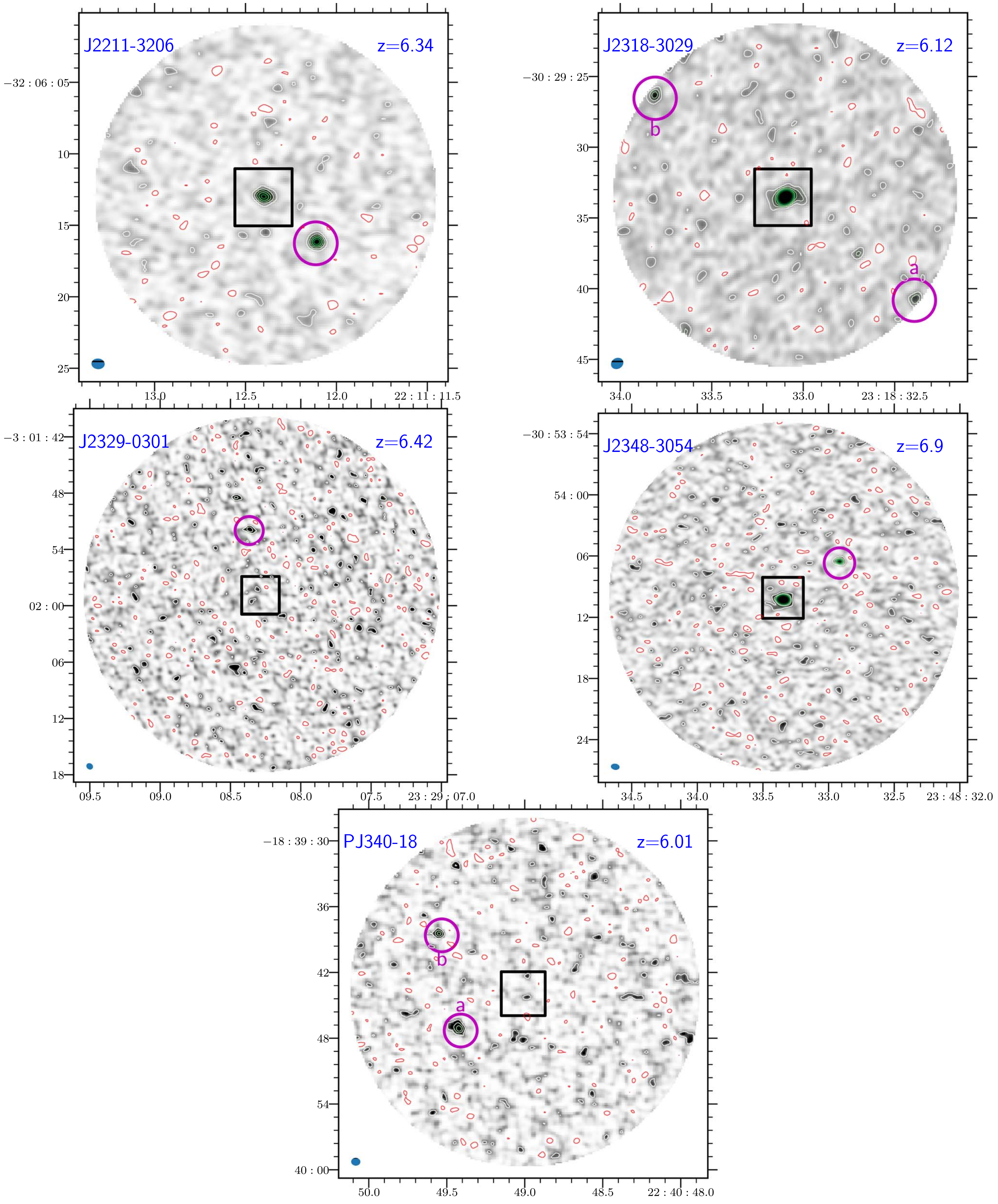

Figure 4. (Continued.)

overdensity further away from the quasar. While one might expect to detect an overdensity by observing within 2–3 cMpc, our 1 Mpc scales are not sufficient to rule out overdensities (though a detected overdensity would have provided sufficient evidence of a more massive structure). This may be especially true if the quasar itself is emitting ionizing radiation, creating an ionized bubble in the so-called near-zone expected to be $\gtrsim$1 pMpc wide (Fan et al. 2006; Eilers et al. 2017), which may suppress galaxy formation in the quasar's immediate vicinity. Numerical simulations (Dubois et al. 2013; Costa et al. 2014;

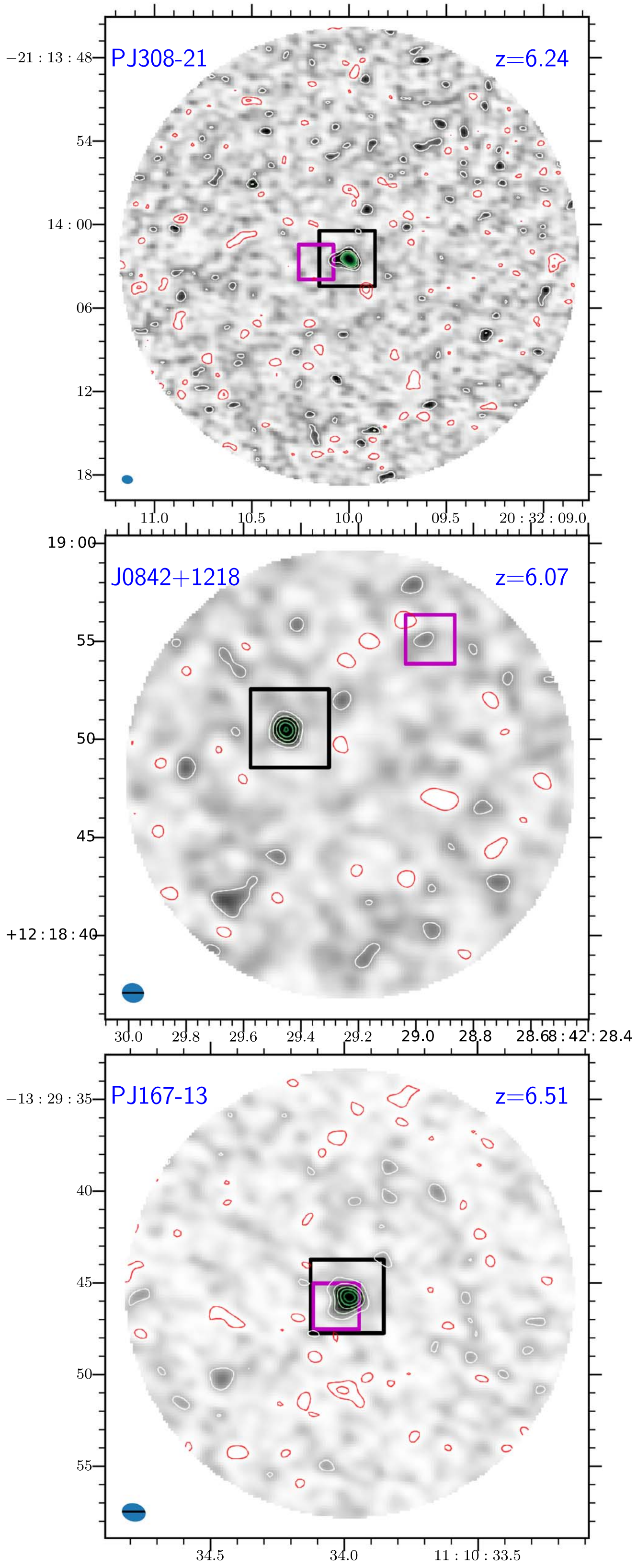

Figure 5. Three fields from this sample in which [C II] (magenta squares) was discovered but no 5σ dust continuum counterpart was discovered in this study. QSOs PJ308–21 and J0842+1218 mark detections from Decarli et al. (2017). QSO PJ167–13 marks a detection from Willott et al. (2017); the quasar has not been masked out in this map due to the close angular proximity of the companion source.

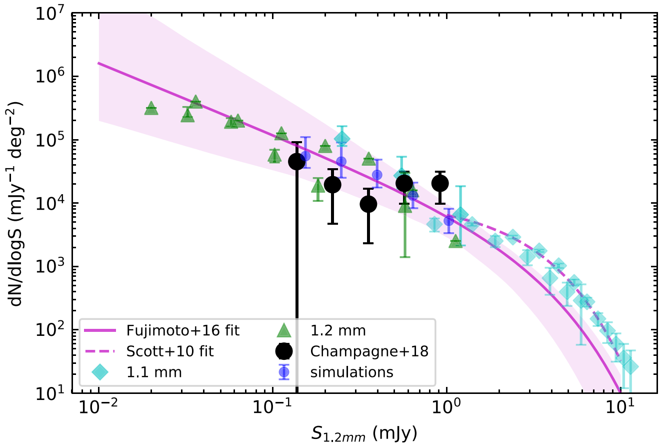

Figure 6. Blank field number counts from previous studies are shown as represented in the legend: Aravena et al. (2016a), Fujimoto et al. (2016), Hatsukade et al. (2016), Oteo et al. (2016), and Scott et al. (2010, 2012). The Schechter fits use the parameters from Fujimoto et al. (2016). The shaded magenta region represents the 16th and 84th percentile bounds on the Monte Carlo simulation based on the Fujimoto et al. (2016) function. The green points correspond to the 1.2 mm number counts, the cyan points correspond to the 1.1 mm number counts, the dark blue points correspond to an average over the 1000 simulated maps we have created according to Fujimoto et al. (2016), and the black points are from this study. These points represent the total number of candidate companions divided by the area of the study to which that flux bin is sensitive. The black points are calculated in six log(flux) bins from 0.1 to 1.5 mJy.

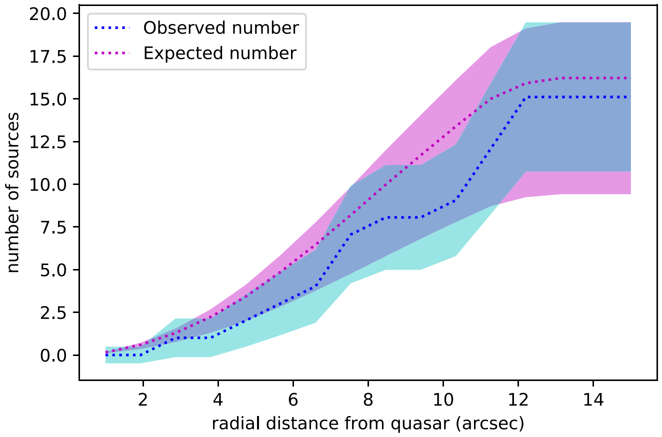

Figure 7. Number of sources as a function of radial distance from the quasar. A_{eff} has been corrected for sensitivity as before, but is calculated based on angular radius rather than the fraction of the primary beam. The magenta line and shaded region shows the number of sources expected and its error based on our simulation. The cyan line and shaded region shows the observed number of sources and associated error. No overdensity arises at any angular separation, showing that our choice of primary beam cut has not influenced our calculation.

Barai et al. 2018) suggest that the most massive quasars at these epochs ($M_{\mathrm{BH}} \gtrsim 10^9\,M_\odot$) may produce significant enough feedback to suppress star formation on hundreds of kpc separation from the quasar, consistent with the present lack of millimeter detections at close angular separations. If this is the case, an excess of dusty star-forming galaxies may not be found on kpc scales near quasars this massive. However, we stress once again that the overdensity of [C II] emitters found by Decarli et al. (2017) suggest that star-forming galaxies are assembling near the quasars, and it is unlikely that any feedback process would eliminate the dust emission but not the

Table 2
List of Properties for the Counterparts in the Quasar Fields

Name (1)	R.A. (J2000) (2)	Decl. (J2000) (3)	Peak Flux (mJy) (4)	S/N (5)	PB Resp. (6)	Offset from Quasar (″) (7)
C–PJ009a	00:38:56.342	−10:26:01.740	0.67 ± 0.16	5.83	0.705	8.3
C–PJ009b	00:38:57.182	−10:25:48.440	0.95 ± 0.32	5.94	0.501	11.3
C–J0046	00:46:23.780	−28:37:51.360	1.47 ± 0.09	17.36	0.916	4.5
C–J0305	03:05:16.374	−31:50:55.000	0.30 ± 0.05	6.18	0.915	7.0
C–PJ231a	15:26:37.877	−20:50:02.520	0.93 ± 0.09	10.18	0.995	1.9
C–PJ231b	15:26:38.185	−20:50:09.940	0.75 ± 0.24	5.10	0.620	10.6
C–J2054	20:54:06.390	−0:05:25.299	0.23 ± 0.06	5.22	0.716	10.6
C–J2100	21:00:54.060	−17:15:29.780	0.68 ± 0.17	7.40	0.525	11.1
C–J2211	22:11:12.113	−32:06:16.260	0.64 ± 0.06	11.74	0.903	4.8
C–PJ340a[a]	22:40:49.410	−18:39:47.300	0.51 ± 0.08	7.48	0.891	7.1
C–PJ340b[a]	22:40:49.531	−18:39:38.620	0.53 ± 0.10	6.86	0.795	9.6
C–J2318a	23:18:32.392	−30:29:40.819	1.02 ± 0.33	5.89	0.521	11.8
C–J2318b	23:18:33.809	−30:29:26.539	1.23 ± 0.32	7.26	0.532	11.6
C–J2329	23:29:08.366	−03:01:51.989	0.14 ± 0.02	5.97	0.921	6.9
C–J2348	23:48:32.917	−30:54:06.700	0.69 ± 0.06	11.96	0.919	6.5

Notes. Field sources identified in the 35 ALMA maps. (1) Names correspond to the short names of the field in which they are detected. (2)–(3) R.A., decl. of each field source. (4) Peak flux is calculated from the brightest pixel in the candidate and is corrected for the primary beam offset. (5) S/N of the peak flux. (6) Primary beam response at the position of the source. (7) Angular offset from the quasar.

[a] Source has a faint, extended counterpart in the K band (∼23 AB mag).

Table 3
Values Calculated for the Differential Number Counts

$\log S_\nu$ (1)	$N_{\rm sources}$ (2)	$dN/d\log S_\nu$ (10^3 mJy^{-1} deg^{-2}) (3)	δN (4)
−0.86	1	45.1	46.8
−0.65	2	19.5	14.8
−0.45	2	9.6	7.3
−0.25	5	20.5	10.8
−0.04	5	20.5	10.7
0.16	…	…	…

Note. Differential number counts as shown in Figure 4. (1) Lower limit of flux density (S_ν) bin. (2) Number of entries per bin (before fidelity and completeness correction). (3) Differential number count (sources per $d\log S_\nu$ per $A_{\rm eff}$), corrected for fidelity and completeness. (4) Errors on $dN/d\log S_\nu$.

gas emission. It is still possible, however, that true overdensities of dust emitters would be traced only on much larger scales (several comoving Mpc). To test this hypothesis, observations targeting a much wider field around quasars are required.

Cosmic Variance. The average ALMA primary beam (∼25″) is not only much smaller than the size of a typical protocluster, but is also significantly smaller than the physical scale of expected density variations in the $z \sim 6$ universe (30–80 Mpc or 0°.25–0°.5; e.g., D'Aloisio et al. 2018). Despite the fact that quasar sightlines are assumed to be biased toward overdense regions, both cosmic variance and Poisson noise contribute to large fluctuations in field-to-field number counts. According to estimates of mass overdensities from protocluster simulations at $z \sim 5$ (e.g., Chiang et al. 2013), $\delta_{\rm gal}$ may vary by a factor of 2–3 between protoclusters, depending on the mass scale of the protocluster and the physical volume probed. This variance rises when the field of view shrinks, so with low numbers of quasars whose individual fields of view are small, it is entirely possible that the field-to-field variation would not amount to an aggregate statistical overdensity due to cosmic variance alone. To combat this, a larger sample size of random quasar sightlines or wide-field mosaicing around one quasar is necessary.

Depth of Observations. These archival observations are fairly shallow (∼10 minutes on source), originally intended to detect the massive host galaxies of the quasar in [C II]. While they are deep enough to detect bright [C II] lines in the quasars and a few companions, our flux limit of 0.15 mJy in continuum corresponds to $L_{\rm IR} \sim 10^{12} L_\odot$ (assuming a modified blackbody SED with $\beta = 1.6$ and $T_d = 35$ K) or an SFR $\approx 40\,M_\odot$ yr^{-1} (Kennicutt & Evans 2012), meaning we will miss more normal star-forming galaxies. To improve upon the small number statistics, we might consider ALMA observations that reach a fainter flux limit than the one in this study, since the slope of the 1.2 mm number counts predicts that sources with $S_\nu < 0.1$ mJy will be more common by an order of magnitude than our current limit. However, because of the strong negative K-correction for sub/millimeter flux, this method would likely introduce many more faint foreground contaminants. Additionally, the faint-end slope of the IR luminosity function (IRLF) is much shallower than that of the UV luminosity function as probed by Lyα (Casey et al. 2014; Finkelstein et al. 2015). Therefore, increased depth may not reveal an overdensity of IR sources currently below the detection threshold, unlike the large effect of depth on UV/optical surveys.

Density of foreground sources. The largest effect on this study is likely the large comoving depth of this search, due to the flat redshift selection of 1.2 mm dust observations. The very negative *K*-correction of the sub/millimeter regime means that sources do not fade with increasing redshift from $z \sim 1-10$ (see Figure 3; Casey et al. 2014), so compared with the narrow redshift ranges for LAE and [C II] overdensity searches, we are probing an enormous line-of-sight volume with potential for many millimeter detections. If we are averaging over Gpc scales along the line of sight, it is likely that clusters and voids at various redshifts will cancel out any potential overdensity signal near the targeted quasars. This is especially true as the cosmic IRLF suggests that dusty IR sources are much more common at redshifts $1 < z < 3$ (Le Floc'h et al. 2005; Gruppioni et al. 2013), so at these wavelengths there are probably many more galaxies in the foreground than at the redshift of the quasars.

Without spectroscopic redshifts, or at the least a strong characterization of the luminosity functions at $z < 5$, our current data do not achieve high enough contrast against the foreground population. Future continuum studies would be aided by strong observational constraints of the number of expected foreground sources in continuum, or by obtaining spectroscopic redshifts before looking for dusty counterparts.

Chiang et al. (2013) uses semi-analytical models of protocluster evolution to predict their overdensity profiles out to $z = 5$ in cubes of $(15\ \mathrm{cMpc})^3$. The profile with the closest analog to this work is for star-forming galaxies with SFR $>1\,M_\odot\,\mathrm{yr}^{-1}$ (although the sources here are likely to be much rarer submillimeter-type galaxies), and assuming the conditions at $z = 5$ are applicable to this work, we use this to predict δ_{gal} in the observations. While the observed overdensity will appear less significant in practice due to the background of sub/millimeter sources, we expect the overdensity to be much higher closer to the density peak, so we may still be able to detect a significant δ_{gal} given these models.

As a first step, we convert from δ_{gal} in Chiang et al. (2013) to a 2D projection in an aperture the size of the ALMA Band 6 primary beam. To estimate the expected number of sources at this redshift, we would ideally use the IRLF at $z = 6$, but as this has not yet been measured (Casey et al. 2018) we assume to the first order an expected volume density of sources matching the $z = 6$ LBG luminosity function found in Finkelstein (2016). After converting the 3D δ_{gal} from Chiang et al. (2013), we expect $N_{\mathrm{gal}} \approx 0.13$ associated sources per primary beam, if the quasar resides at the density peak. Thus, this translates to an estimated 4.5 sources associated with 35 $z = 6$ quasars, or a 2D $\delta_{\mathrm{gal}} \approx 0.3$ when including the expected millimeter foreground sources based on current blank field number counts. This highlights the difficulty in finding true overdensities in the millimeter continuum at high redshift, since δ_{gal} is so easily washed out and difficult to constrain without a firm grasp on the IR field population at comparable epochs. Additionally, since neither the $z = 6$ IRLF nor the galaxy bias for SMGs has been observationally constrained, we need more data to make further predictions. However, if semi-analytical models can even approximately estimate SMG overdensities in protoclusters centered on quasars, observational evidence is within reach with a larger sample size.

In summary, 15 candidate detections at $\geqslant 5\sigma$ in 11 out of 35 ALMA maps centered on $z \sim 6$ quasars do not represent a statistically significant flux excess when compared with the blank field number counts at 1.2 mm with a measured $\delta_{\mathrm{gal}} = -0.07 \pm 0.56$. The discrepancy between this result and the [C II] overdensity found by Decarli et al. (2017) is likely due to the large comoving volume probed by our millimeter continuum study, since we cannot confirm that the detected sources are companions to the quasars unless they had a prior [C II] redshift. We can motivate future tests of the hypothesis that SMGs can exist in protoclusters centered around quasars through much deeper observations, or by substantially widening the field of view through mosaic observations. Deeper observations may reveal fainter [C II] sources as well, enabling us to constrain the redshifts of the sources found in the fields. Another follow-up method of study could be going to shorter wavelengths and searching for LAEs with *HST* grism observations, or searching for counterparts in stellar light using the *James Webb Space Telescope*, which would aid in spectroscopic confirmation. We do not take this result to be evidence that protoclusters at high redshift lack dusty star-forming galaxies, as further observations are required to confirm this result.

We thank the anonymous referee for the insightful comments which helped to improve this paper. J.B.C. and C.M.C. thank the College of Natural Sciences at the University of Texas at Austin for support in addition to NSF grant AST-1714528. D.R. acknowledges support from the national Science Foundation under grant number AST-1614213. B.V. and F.W. acknowledge funding through ERC grants "Cosmic Dawn" and "Cosmic Gas."

This paper makes use of the following ALMA data: ADS/JAO.ALMA: 2011.0.00206.S (PI: R. Wang), 2011.0.00243.S (PI: C. Willott), 2012.1.00882.S (PI: B. Venemans), 2013.1.00273.S (PI: B. Venemans), 2015.1.00997.S (PI: R. Maiolino), and 2015.01115.S (PI: F. Walter). ALMA is a partnership of ESO (representing its member states), NSF (USA), and NINS (Japan), together with NRC (Canada), NSC, ASIAA (Taiwan), and KASI (Republic of Korea), in cooperation with the Republic of Chile. The Joint ALMA Observatory is operated by ESO, AUI/NRAO, and NAOJ.

The National Radio Astronomy Observatory is a facility of the National Science Foundation operated under cooperative agreement by Associated Universities, Inc.

Appendix
Quasar Maps with No Additional Detections

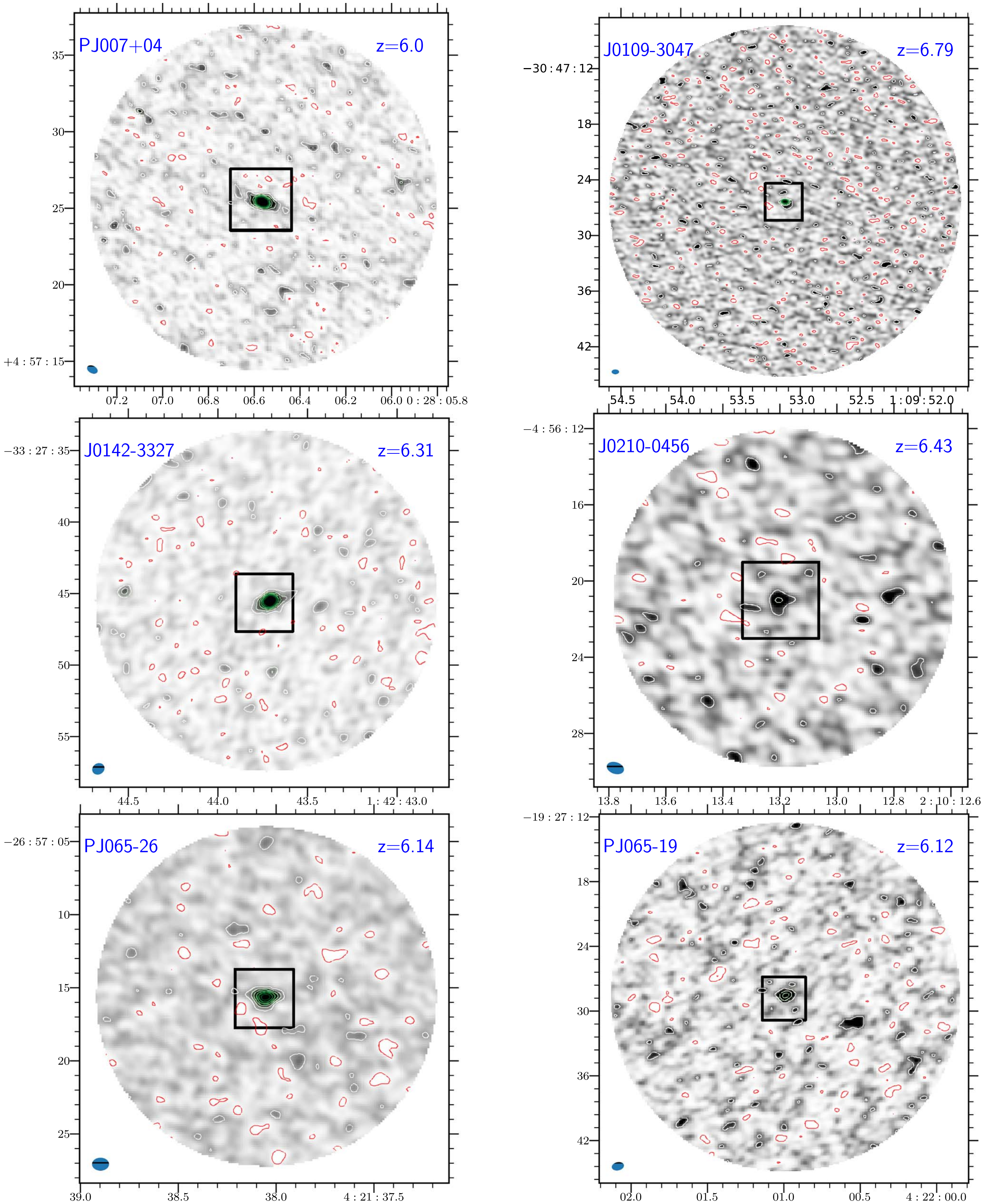

Figure 8. The remaining maps with no continuum or [CII] detections. The figures were created as described in the caption for Figure 4.

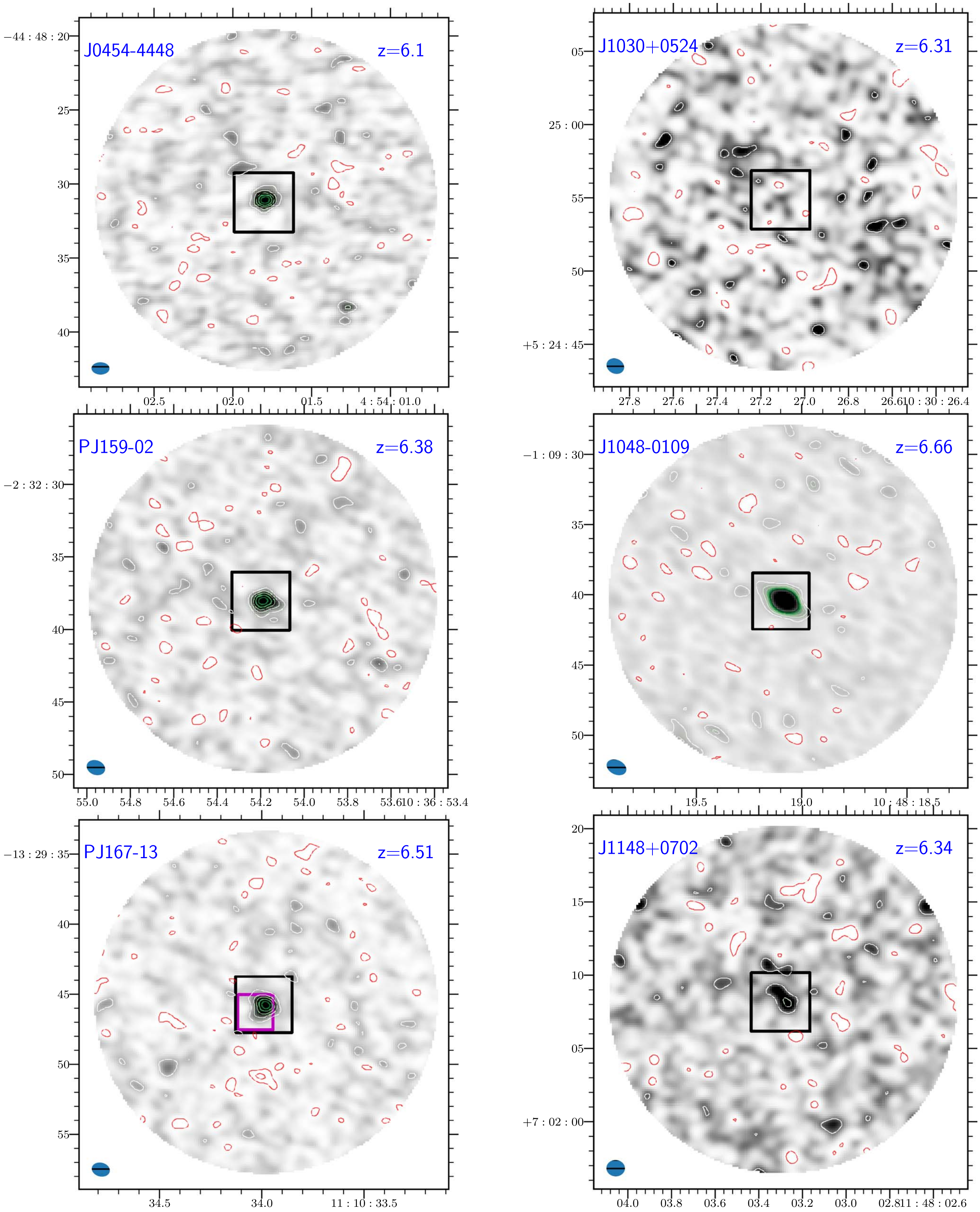

Figure 8. (Continued.)

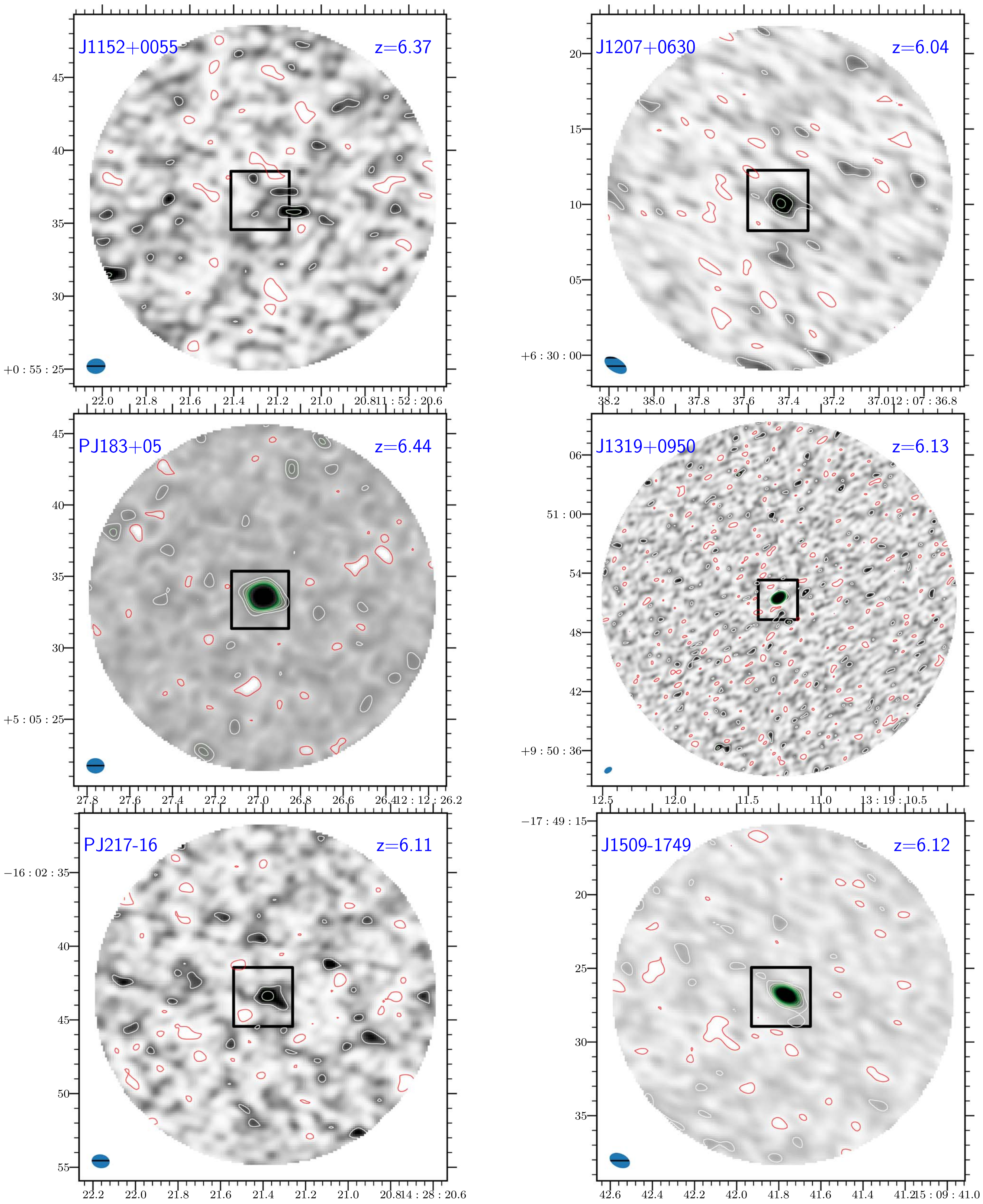

Figure 8. (Continued.)

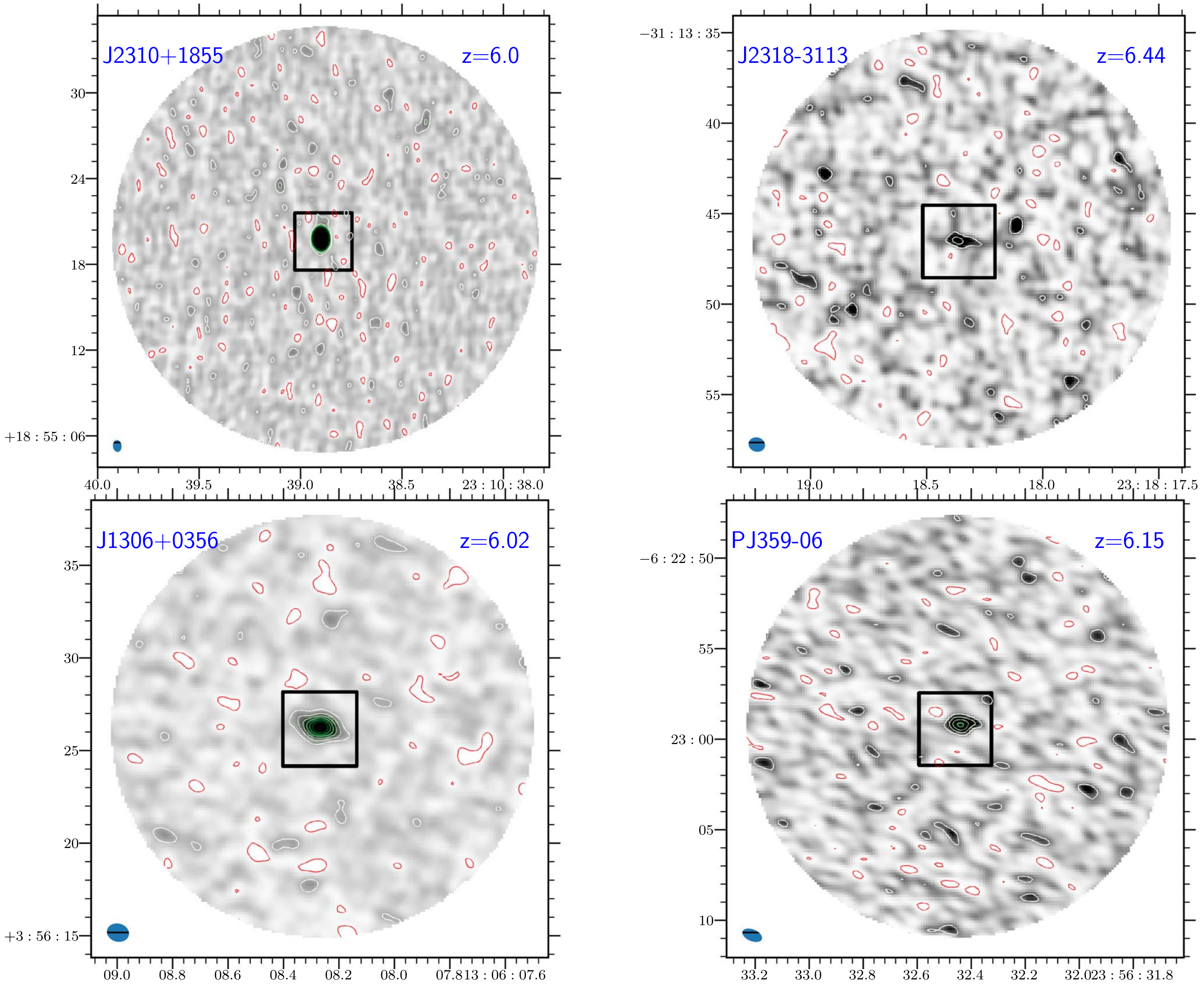

Figure 8. (Continued.)

ORCID iDs

Jaclyn B. Champagne https://orcid.org/0000-0002-6184-9097
Roberto Decarli https://orcid.org/0000-0002-2662-8803
Caitlin M. Casey https://orcid.org/0000-0002-0930-6466
Bram Venemans https://orcid.org/0000-0001-9024-8322
Eduardo Bañados https://orcid.org/0000-0002-2931-7824
Fabian Walter https://orcid.org/0000-0003-4793-7880
Frank Bertoldi https://orcid.org/0000-0002-1707-1775
Xiaohui Fan https://orcid.org/0000-0003-3310-0131
Emanuele Paolo Farina https://orcid.org/0000-0002-6822-2254
Chiara Mazzucchelli https://orcid.org/0000-0002-5941-5214
Dominik A. Riechers https://orcid.org/0000-0001-9585-1462
Michael A. Strauss https://orcid.org/0000-0002-0106-7755
Yujin Yang https://orcid.org/0000-0003-3078-2763

References

Allen, S. W., Evrard, A. E., & Mantz, A. B. 2011, ARA&A, 49, 409
Appenzeller, I., Fricke, K., Fürtig, W., et al. 1998, Msngr, 94, 1
Aravena, M., Decarli, R., Walter, F., et al. 2016a, ApJ, 833, 68
Aravena, M., Decarli, R., Walter, F., et al. 2016b, ApJ, 833, 71
Arnaboldi, M., Neeser, M. J., Parker, L. C., et al. 2007, Msngr, 127, 28
Austermann, J. E., Dunlop, J. S., Perera, T. A., et al. 2010, MNRAS, 401, 160
Bădescu, T., Yang, Y., Bertoldi, F., et al. 2017, ApJ, 845, 172
Bañados, E., Venemans, B., Walter, F., et al. 2013, ApJ, 773, 178
Bañados, E., Venemans, B. P., Decarli, R., et al. 2016, ApJS, 227, 11
Bañados, E., Venemans, B. P., Morganson, E., et al. 2014, AJ, 148, 14
Barai, P., Gallerani, S., Pallottini, A., et al. 2018, MNRAS, 473, 4003
Becker, G. D., Bolton, J. S., & Lidz, A. 2015, PASA, 32, e045
Capak, P. L., Riechers, D., Scoville, N. Z., et al. 2011, Natur, 470, 233
Carilli, C. L., Walter, F., Bertoldi, F., et al. 2004, AJ, 128, 997
Carnall, A. C., Shanks, T., Chehade, B., et al. 2015, MNRAS, 451, L16
Casey, C. M. 2016, ApJ, 824, 36
Casey, C. M., Cooray, A., Capak, P., et al. 2015, ApJL, 808, L33
Casey, C. M., Narayanan, D., & Cooray, A. 2014, PhR, 541, 45
Casey, C. M., Zavala, J. A., Spilker, J., et al. 2018, ApJ, 862, 77
Chambers, K. C., Magnier, E. A., Metcalfe, N., et al. 2016, arXiv:1612.05560
Chapman, S. C., Blain, A., Ibata, R., et al. 2009, ApJ, 691, 560
Chen, S.-F. S., Simcoe, R. A., Torrey, P., et al. 2016, arXiv:1612.02829
Chiang, Y.-K., Overzier, R., & Gebhardt, K. 2013, ApJ, 779, 127
Chiang, Y.-K., Overzier, R. A., Gebhardt, K., & Henriques, B. 2017, ApJL, 844, L23
Costa, T., Sijacki, D., Trenti, M., & Haehnelt, M. G. 2014, MNRAS, 439, 2146
Cowie, L. L., & Hu, E. M. 1986, ApJL, 305, L39
D'Aloisio, A., McQuinn, M., Davies, F. B., & Furlanetto, S. R. 2018, MNRAS, 473, 560
Dark Energy Survey Collaboration, Abbott, T., Abdalla, F. B., et al. 2016, MNRAS, 460, 1270
Decarli, R., Walter, F., Venemans, B. P., et al. 2017, Natur, 545, 457
Decarli, R., Walter, F., Venemans, B. P., et al. 2018, ApJ, 854, 97
Decarli, R., Walter, F., Yang, Y., et al. 2012, ApJ, 756, 150

De Rosa, G., Decarli, R., Walter, F., et al. 2011, ApJ, 739, 56
Djorgovski, S., Spinrad, H., McCarthy, P., & Strauss, M. A. 1985, ApJL, 299, L1
Dubois, Y., Pichon, C., Devriendt, J., et al. 2013, MNRAS, 428, 2885
Eilers, A.-C., Davies, F. B., Hennawi, J. F., et al. 2017, ApJ, 840, 24
Fan, X., Narayanan, V. K., Lupton, R. H., et al. 2001, AJ, 122, 2833
Fan, X., Strauss, M. A., Becker, R. H., et al. 2006, AJ, 132, 117
Fan, X., Strauss, M. A., Schneider, D. P., et al. 2003, AJ, 125, 1649
Farina, E. P., Venemans, B. P., Decarli, R., et al. 2017, ApJ, 848, 78
Finkelstein, S. L. 2016, PASA, 33, e037
Finkelstein, S. L., Ryan, R. E., Jr., Papovich, C., et al. 2015, ApJ, 810, 71
Fujimoto, S., Ouchi, M., Ono, Y., et al. 2016, ApJS, 222, 1
Goto, T., Utsumi, Y., Kikuta, S., et al. 2017, MNRAS, 470, L117
Gruppioni, C., Pozzi, F., Rodighiero, G., et al. 2013, MNRAS, 432, 23
Hatsukade, B., Kohno, K., Umehata, H., et al. 2016, PASJ, 68, 36
Hayashi, M., Kodama, T., Tadaki, K.-i., Koyama, Y., & Tanaka, I. 2012, ApJ, 757, 15
Hodge, J. A., Swinbank, A. M., Simpson, J. M., et al. 2016, ApJ, 833, 103
Hung, C.-L., Casey, C. M., Chiang, Y.-K., et al. 2016, ApJ, 826, 130
Jiang, L., Fan, X., Hines, D. C., et al. 2006, AJ, 132, 2127
Jiang, L., McGreer, I. D., Fan, X., et al. 2015, AJ, 149, 188
Jiang, L., McGreer, I. D., Fan, X., et al. 2016, ApJ, 833, 222
Kennicutt, R. C., & Evans, N. J. 2012, ARA&A, 50, 531
Kim, S., Stiavelli, M., Trenti, M., et al. 2009, ApJ, 695, 809
Koyama, Y., Kodama, T., Nakata, F., Shimasaku, K., & Okamura, S. 2011, ApJ, 734, 66
Kravtsov, A. V., & Borgani, S. 2012, ARA&A, 50, 353
Kuiper, E., Hatch, N. A., Venemans, B. P., et al. 2011, MNRAS, 417, 1088
Kurk, J. D., Walter, F., Fan, X., et al. 2007, ApJ, 669, 32
Kurk, J. D., Walter, F., Fan, X., et al. 2009, ApJ, 702, 833
Larson, R. L., Finkelstein, S. L., Pirzkal, N., et al. 2018, ApJ, 858, 94
Lawrence, A., Warren, S. J., Almaini, O., et al. 2007, MNRAS, 379, 1599
Le Floc'h, E., Papovich, C., Dole, H., et al. 2005, ApJ, 632, 169
Lewis, I., Balogh, M., De Propris, R., et al. 2002, MNRAS, 334, 673
Madau, P., Haardt, F., & Dotti, M. 2014, ApJL, 784, L38
Matsuoka, Y., Onoue, M., Kashikawa, N., et al. 2016, ApJ, 828, 26
Mazzucchelli, C., Bañados, E., Decarli, R., et al. 2017a, ApJ, 834, 83
Mazzucchelli, C., Bañados, E., Venemans, B. P., et al. 2017b, ApJ, 849, 91
McMullin, J. P., Waters, B., Schiebel, D., Young, W., & Golap, K. 2007, in ASP Conf. Ser. 376, Astronomical Data Analysis Software and Systems XVI, ed. R. A. Shaw, F. Hill, & D. J. Bell (San Francisco, CA: ASP), 127
Miley, G. K., Overzier, R. A., Tsvetanov, Z. I., et al. 2004, Natur, 427, 47
Miyazaki, S., Komiyama, Y., Sekiguchi, M., et al. 2002, PASJ, 54, 833
Morselli, L., Mignoli, M., Gilli, R., et al. 2014, A&A, 568, A1
Mortlock, D. J., Patel, M., Warren, S. J., et al. 2009, A&A, 505, 97
Mortlock, D. J., Patel, M., Warren, S. J., et al. 2012, MNRAS, 419, 390
Narayanan, D., Turk, M., Feldmann, R., et al. 2015, Natur, 525, 496
Ota, K., Venemans, B. P., Taniguchi, Y., et al. 2018, ApJ, 856, 109
Oteo, I., Zwaan, M. A., Ivison, R. J., Smail, I., & Biggs, A. D. 2016, ApJ, 822, 36
Overzier, R. A. 2016, A&ARv, 24, 14
Overzier, R. A., Guo, Q., Kauffmann, G., et al. 2009, MNRAS, 394, 577
Palunas, P., Teplitz, H. I., Francis, P. J., Williger, G. M., & Woodgate, B. E. 2004, ApJ, 602, 545
Pâris, I., Petitjean, P., Ross, N. P., et al. 2017, A&A, 597, A79
Pentericci, L., Fan, X., Rix, H.-W., et al. 2002, AJ, 123, 2151
Pezzulli, E., Valiante, R., Orofino, M. C., et al. 2017, MNRAS, 466, 2131
Planck Collaboration, Ade, P. A. R., Aghanim, N., et al. 2016, A&A, 594, A13
Pont, F., Hébrard, G., Irwin, J. M., et al. 2009, A&A, 502, 695
Reed, S. L., McMahon, R. G., Banerji, M., et al. 2015, MNRAS, 454, 3952
Reed, S. L., McMahon, R. G., Martini, P., et al. 2017, MNRAS, 468, 4702
Riechers, D. A., Carilli, C. L., Capak, P. L., et al. 2014, ApJ, 796, 84
Schechter, P. 1976, ApJ, 203, 297
Scott, K. S., Wilson, G. W., Aretxaga, I., et al. 2012, MNRAS, 423, 575
Scott, K. S., Yun, M. S., Wilson, G. W., et al. 2010, MNRAS, 405, 2260
Shanks, T., Metcalfe, N., Chehade, B., et al. 2015, MNRAS, 451, 4238
Shimasaku, K., Ouchi, M., Okamura, S., et al. 2003, ApJL, 586, L111
Sijacki, D., Vogelsberger, M., Genel, S., et al. 2015, MNRAS, 452, 575
Skibba, R. A., Bamford, S. P., Nichol, R. C., et al. 2009, MNRAS, 399, 966
Springel, V. 2005, MNRAS, 364, 1105
Springel, V., White, S. D. M., Jenkins, A., et al. 2005, Natur, 435, 629
Steidel, C. C., Adelberger, K. L., Dickinson, M., et al. 1998, ApJ, 492, 428
Steidel, C. C., Adelberger, K. L., Shapley, A. E., et al. 2005, ApJ, 626, 44
Stevens, J. A., Ivison, R. J., Dunlop, J. S., et al. 2003, Natur, 425, 264
Stiavelli, M., Djorgovski, S. G., Pavlovsky, C., et al. 2005, ApJL, 622, L1
Swinbank, A. M., Karim, A., Smail, I., et al. 2012, MNRAS, 427, 1066
Toshikawa, J., Uchiyama, H., Kashikawa, N., et al. 2018, PASJ, 70, 12
Trakhtenbrot, B., Lira, P., Netzer, H., et al. 2018, arXiv:1801.01508
Treu, T., Schmidt, K. B., Trenti, M., Bradley, L. D., & Stiavelli, M. 2013, ApJL, 775, L29
Venemans, B. 2015, Natur, 518, 490
Venemans, B. P. 2007, in ASP Conf. Ser. 379, Cosmic Frontiers, ed. N. Metcalfe & T. Shanks (San Francisco, CA: ASP), 43
Venemans, B. P., Bañados, E., Decarli, R., et al. 2015a, ApJL, 801, L11
Venemans, B. P., Findlay, J. R., Sutherland, W. J., et al. 2013, ApJ, 779, 24
Venemans, B. P., Kurk, J. D., Miley, G. K., et al. 2002, ApJL, 569, L11
Venemans, B. P., McMahon, R. G., Walter, F., et al. 2012, ApJL, 751, L25
Venemans, B. P., McMahon, R. G., Warren, S. J., et al. 2007a, MNRAS, 376, L76
Venemans, B. P., Röttgering, H. J. A., Miley, G. K., et al. 2005b, A&A, 431, 793
Venemans, B. P., Röttgering, H. J. A., Miley, G. K., et al. 2007b, A&A, 461, 823
Venemans, B. P., Röttgering, H. J. A., Overzier, R. A., et al. 2004, A&A, 424, L17
Venemans, B. P., Verdoes Kleijn, G. A., Mwebaze, J., et al. 2015c, MNRAS, 453, 2259
Venemans, B. P., Walter, F., Decarli, R., et al. 2017a, ApJ, 845, 154
Venemans, B. P., Walter, F., Decarli, R., et al. 2017b, ApJ, 837, 146
Venemans, B. P., Walter, F., Zschaechner, L., et al. 2016, ApJ, 816, 37
Walter, F., Bertoldi, F., Carilli, C., et al. 2003, Natur, 424, 406
Wang, R., Carilli, C. L., Neri, R., et al. 2010, ApJ, 714, 699
Wang, R., Carilli, C. L., Wagg, J., et al. 2008, ApJ, 687, 848
Wang, R., Wagg, J., Carilli, C. L., et al. 2013, ApJ, 773, 44
Willott, C. J., Bergeron, J., & Omont, A. 2017, ApJ, 850, 108
Willott, C. J., Delfosse, X., Forveille, T., Delorme, P., & Gwyn, S. D. J. 2005, ApJ, 633, 630
Willott, C. J., Delorme, P., Omont, A., et al. 2007, AJ, 134, 2435
Willott, C. J., Delorme, P., Reylé, C., et al. 2009, AJ, 137, 3541
Willott, C. J., Delorme, P., Reylé, C., et al. 2010, AJ, 139, 906
Willott, C. J., Omont, A., & Bergeron, J. 2013, ApJ, 770, 13
Wylezalek, D., Galametz, A., Stern, D., et al. 2013, ApJ, 769, 79
Xu, W., Fang, L.-Z., & Wu, X.-P. 2000, ApJ, 532, 728